The numerical scheme of the discrete sources method to analyze 3D plasmonic nanostructures accounting for the non-local effect

Yuri Eremin [a], Adrian Doicu [b], Thomas Wriedt [c,*]

[a] *Lomonosov Moscow State University, Lenin's Hills, 119991 Moscow, Russia*
[b] *Remote Sensing Technology Institute German Aerospace Centre (DLR), Oberpfaffenhofen, Germany*
[c] *Leibniz-Institut für Werkstofforientierte Technologien - IWT, University of Bremen, Bremen, Germany*

ARTICLE INFO

ABSTRACT

We present an extension of the discrete sources method for solving the time-harmonic Maxwell equations accounting for the non-local effect. The developed numerical scheme coupling the non-local hydrodynamic Drude model and the generalized non-local optical response model is described in detail. Numerical results computed for a single non-spherical particle and a linear dimer are presented. Our results demonstrate that the discrete sources method can be efficiently used to model the non-local effect in a wide range of 3D scattering problems.

© 2019 Elsevier Inc. All rights reserved.

1. Introduction

Nanophotonics is an active research field concerned with the study of interactions between nanometer scale structures and light, including near-infrared, visible, and ultraviolet light. Owing to the rapid progress in fabrication, characterization, and surface functionalization technologies there are many potential applications including invisibility cloaking, nanoantennas, metamaterials, novel biological detection technologies, as well as, new optical storage concepts [1,2]. Plasmonics in nanophotonics deals with the study of the collective oscillations of free electrons in nobel metals that can be resonantly excited at optical frequencies. These oscillations exhibit unique optical properties across the light spectrum and have been extensively studied for their ability to enhance the incident field intensity by several orders of magnitude [3].

At nanometer or even sub-nanometer scale, metallic structures operating at optical frequencies demonstrate interesting features that are increasingly exploited in the area of nanophotonics [4]. To be able to optimize these enhanced properties for a specific application, appropriate modeling tools are required, in particular, to describe the reaction of the electrons in the metal subjected to an incident electromagnetic wave [5]. If the feature size is lower than the mean free path of the conduction electrons, the electron scattering rate at the feature surface increase. At these scales and with optical frequencies considered, the classical description of the propagation of an electromagnetic wave is no longer valid, because additionally, the electric spatial dispersion of the metal has to be taken into account [6,7]. At sub-nanometer scales, it appears that

---

* Corresponding author.
  E-mail address: thw@iwt.uni-bremen.de (T. Wriedt).

quantum effects must be taken into account because the electron behavior depends not only on the field at the position of the electron (local response approximation (LRA)), but also on the neighboring field distribution (non-local effect) [8]. If the structure size is less than approximately 10 nm, or there is a sharp variation in the surface topography, the classical Maxwell theory is no longer sufficient and a new approach going beyond classical electromagnetics that can describe the occurring physical effects is required. Currently, the most popular approaches accounting for the non-local effect are the Hydrodynamic Drude theory (HDD) [9,10] and the Generalized Non-local Optical Response (GNOR) concept that consider the equation for the free electron motion inside the particle, and for the electron diffusion in the case of GNOR [11–13]. Besides the theories mentioned above, some approximate approaches that enable to treat plasmonic nanostructures accounting for the NLE are also available [14–16].

Except for some highly symmetric structures geometries (circular cylinders or spheres), analytical solutions to the Maxwell equations are not available. Thus, a numerical treatment is an important aspect of nanophotonics research. Numerical experiments help to find new promising nano-systems and geometries prior to real fabrication, to obtain optimized parameters, to visualize the field distributions, to investigate the dominant contribution to a phenomenon under consideration, and finally, to interpret the results of experimental observations [4]. To provide reliable, accurate, and controllable simulation results, a computer based electromagnetic model should account for all features of interaction in the plasmonic structures down to ångstrom dimension. Besides the computation time and memory requirements, a numerical method is characterized by the ease of implementation, the complexity of discretization, and versatility. Some numerical methods can be applied to handle a broad range of plasmonic systems, while others are very efficient for some specific problems. In fact, for a physicist or an engineer, a compromise between the solvable spectrum of problems and the availability of specific numerical methods has usually to be found [17].

The numerical methods that are commonly used in plasmonics can be divided into two groups.

1. Direct methods which are directly applicable to the system of Maxwell equations. In this category, we include the Finite Difference Time Domain (FDTD) method [18] working in the time domain, and the Finite Elements Method (FEM) [19] operating in the frequency domain. The FDTD method is one of the most popular methods in nanophotonics because of its easy concept and its ability to handle a wide variety of problems. In this method, the time and the space are discretized, and the spatial and temporal derivatives appearing in the Maxwell equations are replaced by their finite-difference counterparts. More recently, the Discontinuous Galerkin Time-Domain (DGTD) method has drawn a lot of attention because of several appealing features, as for example, an ease of adaptation to complex geometries and material composition, high-order accuracy, and natural parallelism [20]. The FEM is another popular method in nanophotonics, which allows for an accurate computation of the electromagnetic field in the frequency domain. In very recent years, the Hybridizable Discontinuous Galerkin (HDG) method appears to be a promising numerical method for time-harmonic problems because it inherits nearly all the advantages of the discontinuous Galerkin methods while leading to a computational complexity similar to FEM [21,22].
2. Semi-analytical methods which use the Green theorem to reduce the boundary value problem to an inhomogeneous domain. In this category, we include (i) volume based methods, as for example, the Volume Integral Equations (VIE) method [23] and the Discrete Dipole Approximation (DDA) [24], and (ii) surface based methods, as for example, the Surface Integral Equations (SIE) method [17], the Boundary Element Method (BEM) [25], the T-matrix approach [26], the Multiple MultiPole (MMP) Method [27], and the Discrete Sources Method (DSM) [28].

For nanophotonic structures consisting of homogeneous plasmonic particles, surface based methods seem to be the most appropriate [17,27]. The reason is that when accounting for the non-local response, these methods (i) are able to solve a vector Helmholtz equation with a very large wavenumber, and (ii) can handle very small discretization steps. In this regard, we like to mention that the discretization is determined by the Fermi wavelength; for Ag particle, the Fermi wavelength $v_F = 0.52$ nm requires a discretization step smaller than 0.05 nm to achieve a reasonable accuracy [29]. At present, there are a number of papers in which the numerical scheme for analyzing nanophotonic structures with NLE is described in detail [30–33], but at the same time, most of the associated numerical results have been obtained for cylindrical structures, that is, for the case of a 2D scattering problem only.

The Discrete Sources Method (DSM) we developed is a semi-analytical surface based method, in which the electromagnetic fields are constructed as linear combinations of fields of discrete sources (DS), whose amplitudes are determined from the boundary conditions enforced at the particle surfaces. As compared to other surface-based approaches, the numerical scheme of the DSM has some preferences: (i) it does not require any mesh generation or an integration procedure over the particle surface, (ii) it provides the near and far fields in clear analytical form, (iii) it simultaneously solves the scattering problem for all incident directions and polarizations at once, (iv) it allows to handle particles with high refractive indices by using different numbers of discrete sources for representing the scattered and internal fields, and (v) it ensures an exclusive opportunity to estimate the computational errors via the residual of the surface fields [28]. The resulting computer models are low in computational demand, flexible, and easy to use. These theoretical and numerical advantages recommend the DSM for analyzing 3D plasmonic nanostructures in the presence of NLE [29,34].

In this paper we present how non-local models are handled in the framework of the discrete sources method (Sections 2 and 3), the corresponding numerical scheme (Section 2), and finally, some computational results for spheroids and dimers of spheroids.
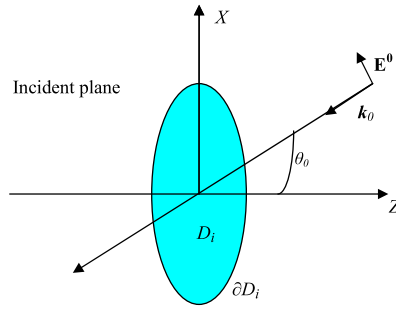
Fig. 1. Scattering problem geometry.

2. Non-local models

We consider scattering of an electromagnetic plane wave ($\mathbf{E}_0, \mathbf{H}_0$) by an axisymmetric homogeneous metallic particle placed in an isotropic homogeneous dielectric medium as shown in Fig. 1. The particle occupies the domain D_i with smooth boundary $S_i = \partial D_i$. By assumption, the media are nonmagnetic, and the axis of symmetry of the particle is aligned with the Oz axis. The incident plane electromagnetic wave propagates in the Oxz plane along a direction which encloses the angle $\pi - \theta_0$ with respect to the Oz axis.

A model for simulating the non-local effect can be characterized as follows.

1. The local-response Ohm law in the metallic particle $\mathbf{J}_i(\mathbf{r}) = \sigma \mathbf{E}_i(\mathbf{r})$ is corrected for non-local dynamics as [7]

$$\frac{\xi^2}{\varepsilon_b} \nabla[\nabla \cdot \mathbf{J}_i(\mathbf{r})] + \mathbf{J}_i(\mathbf{r}) = \sigma \mathbf{E}_i(\mathbf{r}), \tag{1}$$

where for a time dependence of the fields we use $\exp(j\omega t)$,

$$\xi_{\mathrm{HDD}}^2 = \varepsilon_b \left[\frac{\beta^2}{\omega(\omega - j\gamma)} \right], \quad \xi_{\mathrm{GNOR}}^2 = \varepsilon_b \left[\frac{\beta^2}{\omega(\omega - j\gamma)} + j\frac{D}{\omega} \right], \tag{2}$$

where ε_b the permittivity associated to bound charges, ω the frequency, $\beta^2 = (3/5)v_F^2$, v_F the Fermi velocity, γ the Drude damping rate, D the diffusion constant, and σ the Drude conductivity.

2. The Maxwell equation for the magnetic field reads as

$$\nabla \times \mathbf{H}_i(\mathbf{r}) = j\omega\varepsilon_0[\varepsilon_i + \xi^2 \nabla(\nabla \cdot)]\mathbf{E}_i(\mathbf{r}), \tag{3}$$

where

$$\varepsilon_i = \varepsilon_b - \frac{\omega_p^2}{\omega^2 - j\gamma\omega} \tag{4}$$

is the Drude permittivity, ε_0 the vacuum permittivity, and ω_p the plasma frequency of the metal.

3. The field in the metal $\mathbf{E}_i$ sums the contributions of a divergence-free transverse field $\mathbf{E}_{Ti}$ and a curl-free longitudinal field $\mathbf{E}_{Li}$ solving the vector Helmholtz equation with wavenumbers $k_T^2 = k_0^2 \varepsilon_i$ and $k_L^2 = \varepsilon_i/\xi^2$, respectively, where $k_0 = \frac{\omega}{c}$ is the wavenumber in vacuum.

4. The amplitude of the longitudinal wave is computed from the additional boundary condition [7,16]

$$\varepsilon_e \widehat{\mathbf{n}} \cdot [\mathbf{E}_e(\mathbf{r}) + \mathbf{E}_0(\mathbf{r})] = \varepsilon_b \widehat{\mathbf{n}} \cdot \mathbf{E}_i(\mathbf{r}), \tag{5}$$

which is imposed at the interface between the dielectric background medium and the metallic particle. Here, ε_e is the permittivity of the background dielectric medium, $\mathbf{E}_e$ is the scattered field, and $\mathbf{E}_0$ is the incident field; thus $\mathbf{E}_e + \mathbf{E}_0$ is the total field in the background dielectric medium. This boundary condition is used together with the continuity of the tangential components of the electric and magnetic fields at the interface.

In the framework of LRA, when non-local effects are neglected, the conventional equations are obtained by setting $\xi = 0$ in (1) and (3), and by ignoring the longitudinal field (and so, the additional boundary condition (5)).

Considering the scattering problem illustrated in Fig. 1, we are faced with the following boundary value problem: Given the incident electromagnetic field ($\mathbf{E}_0, \mathbf{H}_0$), compute the scattered field ($\mathbf{E}_e, \mathbf{H}_e$) in $D_e = \mathbb{R}^3 \setminus \overline{D_i}$ and the internal field ($\mathbf{E}_i, \mathbf{H}_i$) in D_i, satisfying the Maxwell equations

$$\nabla \times \mathbf{H}_e = jk_0 \varepsilon_e \mathbf{E}_e, \quad \nabla \times \mathbf{E}_e = -jk_0 \mathbf{H}_e, \text{ in } D_e \tag{6}$$

$$\nabla \times \mathbf{H}_i = jk_0 [\varepsilon_i + \xi^2 \nabla (\nabla \cdot)] \mathbf{E}_i, \quad \nabla \times \mathbf{E}_i = -jk_0 \mathbf{H}_i, \text{ in } D_i, \tag{7}$$

and the boundary conditions at the particle surface S_i,

$$\widehat{\mathbf{n}} \times (\mathbf{E}_i - \mathbf{E}_e) = \widehat{\mathbf{n}} \times \mathbf{E}_0, \tag{8}$$

$$\widehat{\mathbf{n}} \times (\mathbf{H}_i - \mathbf{H}_e) = \widehat{\mathbf{n}} \times \mathbf{H}_0, \tag{9}$$

$$\varepsilon_b \widehat{\mathbf{n}} \cdot \mathbf{E}_i = \varepsilon_e \widehat{\mathbf{n}} \cdot (\mathbf{E}_e + \mathbf{E}_0). \tag{10}$$

In addition, the scattered field must satisfy the Silver-Müller radiation condition. As already mentioned, the field inside the particle is decomposed as

$$\mathbf{E}_i = \mathbf{E}_{Ti} + \mathbf{E}_{Li}, \tag{11}$$

where $\mathbf{E}_{Ti}$ and $\mathbf{E}_{Li}$ are respectively, the transverse and longitudinal fields satisfying the following conditions

$$\nabla \cdot \mathbf{E}_{Ti}(\mathbf{r}, \omega) = 0 \text{ and } \nabla \times \mathbf{E}_{Li}(\mathbf{r}, \omega) = 0. $$

3. Discrete sources method

In the frame of the discrete sources method, the electromagnetic fields are constructed as finite linear combinations of the fields produced by dipoles and multipoles distributed over an axis of symmetry 0Z inside the particle. Thus, the solution satisfies the Maxwell equations and the radiation conditions analytically. The unknown amplitudes of the discrete sources are determined from the boundary conditions enforced at the particle surface S_i. In this section we describe a modified scheme of the discrete sources method for modeling the nonlocal optical response.

For the incident electromagnetic plane wave

$$\mathbf{E}_0(\mathbf{r}) = \widehat{\mathbf{e}}_0 e^{-j\mathbf{k}_e \cdot \mathbf{r}} \tag{12}$$

propagating along the direction $(\pi - \theta_0, \pi)$ and being characterized by the wave vector $\mathbf{k}_e = k_e \widehat{\mathbf{k}}_e$, $k_e = k_0 \sqrt{\varepsilon_e}$ and polarization unit vector $\widehat{\mathbf{e}}_0$, the corresponding P- and S-polarized incident fields are given respectively, by

$$\mathbf{E}_0^P(\mathbf{r}) = (\cos\theta_0 \widehat{\mathbf{e}}_x + \sin\theta_0 \widehat{\mathbf{e}}_z) \psi(x, z), \tag{13}$$

$$\mathbf{H}_0^P(\mathbf{r}) = -\sqrt{\varepsilon_e} \widehat{\mathbf{e}}_y \psi(x, z), \tag{14}$$

and

$$\mathbf{E}_0^S(\mathbf{r}) = \widehat{\mathbf{e}}_y \psi(x, z), \tag{15}$$

$$\mathbf{H}_0^S(\mathbf{r}) = \sqrt{\varepsilon_e} (\cos\theta_0 \widehat{\mathbf{e}}_x + \sin\theta_0 \widehat{\mathbf{e}}_z) \psi(x, z), \tag{16}$$

where $(\widehat{\mathbf{e}}_x, \widehat{\mathbf{e}}_y, \widehat{\mathbf{e}}_z)$ are the Cartesian unit vectors and

$$\psi(x, z) = e^{-jk_e(x \sin\theta_0 - z \cos\theta_0)}. \tag{17}$$

For an axisymmetric particle, the P- and S-polarized excitations are treated separately. To account for axial symmetry, we expand each polarized plane wave into a Fourier series in the azimuthal angle φ by using the basic result

$$e^{\pm jx\cos\varphi} = \sum_{m=0}^{\infty} (2 - \delta_{m0})(\pm j)^m J_m(x) \cos m\varphi, \tag{18}$$

where J_m are the cylindrical Bessel functions, and δ_{m0} the Kronecker delta symbol. The scattering problem then decouples over the azimuthal modes m, and a separate solution for each m is obtained.

The discrete sources are placed on the axis Oz (the axis of symmetry of the particle), and in this regard, we denote by $\{z_n^e\}_{n=1}^{N_e^m}$ the positions of the discrete sources for the representation of scattered field, by $\{z_n^T\}_{n=1}^{N_T^m}$ the positions of the discrete sources for representing the transverse field inside the particle, and finally, by $\{z_n^L\}_{n=1}^{N_L^m}$ the positions of the discrete sources for representing the longitudinal field inside the particle. Note that the numbers of discrete sources N_e^m, N_T^m and N_L^m may be different and that they depend on the azimuthal mode number m.

For approximating the transverse field, the fields of the discrete sources are constructed from the vector potentials $\mathbf{A}_{mn}^1$, $\mathbf{A}_{mn}^2$, and $\mathbf{A}_{mn}^3$, defined by:

$$\mathbf{A}_{mn}^{1e,i}(\mathbf{r}) = \Phi_m^{e,i}(\boldsymbol{\varrho}, z_n^{e,T}) \cos[(m+1)\varphi] \widehat{\mathbf{e}}_\varphi$$
$$- \Phi_m^{e,i}(\boldsymbol{\varrho}, z_n^{e,T}) \sin[(m+1)\varphi] \widehat{\mathbf{e}}_\rho, \tag{19}$$

$$\mathbf{A}_{mn}^{2e,i}(\mathbf{r}) = \Phi_m^{e,i}(\boldsymbol{\varrho}, z_n^{e,T}) \sin[(m+1)\varphi] \widehat{\mathbf{e}}_\varphi$$
$$+ \Phi_m^{e,i}(\boldsymbol{\varrho}, z_n^{e,T}) \cos[(m+1)\varphi] \widehat{\mathbf{e}}_\rho, \tag{20}$$

$$\mathbf{A}_{mn}^{3e,i}(\mathbf{r}) = \Phi_0^{e,i}(\boldsymbol{\varrho}, z_n^{e,T}) \widehat{\mathbf{e}}_z, \tag{21}$$

where

$$\Phi_m^e(\boldsymbol{\varrho}, z_n^e) = h_m^{(2)}(k_e R_{z_n^e}) \Big(\frac{\rho}{R_{z_n^e}} \Big)^m, \tag{22}$$

$$\Phi_m^i(\boldsymbol{\varrho}, z_n^T) = j_m(k_T R_{z_n^T}) \Big(\frac{\rho}{R_{z_n^T}} \Big)^m, \tag{23}$$

$k_T = k_0 \sqrt{\varepsilon_i}$, $\boldsymbol{\varrho} = (\rho, z)$, $\rho^2 = x^2 + y^2$, and

$$R_{z_n}^2 = \rho^2 + (z - z_n)^2. \tag{24}$$

For approximating the longitudinal field, the fields of the discrete sources are constructed from the scalar potentials Ψ_{mn} and Ψ_n; for a P-polarized excitation, they defined by

$$\Psi_{mn}(\mathbf{r}) = \Psi_{m+1}(\boldsymbol{\varrho}, z_n^L) \cos[(m+1)\varphi], \tag{25}$$

$$\Psi_n(\mathbf{r}) = \Psi_0(\boldsymbol{\varrho}, z_n^L), \tag{26}$$

where

$$\Psi_m(\boldsymbol{\varrho}, z_n^L) = j_m(k_L R_{z_n^L}) \Big(\frac{\rho}{R_{z_n^L}} \Big)^m, \tag{27}$$

and $k_L^2 = \varepsilon_i / \xi^2$. In this regard, for a P-polarized excitation, the approximate solution is given by

$$\mathbf{E}_{e,Ti}^{\mathcal{N}}(\mathbf{r}) = \sum_{m=0}^{M} \sum_{n=1}^{N_{e,T}^m} p_{mn}^{e,T} \frac{j}{k_0 \varepsilon_{e,i}} \nabla \times \nabla \times \mathbf{A}_{mn}^{1e,i}(\mathbf{r}) + q_{mn}^{e,T} \frac{j}{\varepsilon_{e,i}} \nabla \times \mathbf{A}_{mn}^{2e,i}(\mathbf{r})$$
$$+ \sum_{n=1}^{N_{e,T}^0} r_n^{e,T} \frac{j}{k_0 \varepsilon_{e,i}} \nabla \times \nabla \times \mathbf{A}_n^{3e,i}(\mathbf{r}), \tag{28}$$

$$\mathbf{E}_{Li}^{\mathcal{N}}(\mathbf{r}) = \sum_{m=0}^{M} \sum_{n=1}^{N_L^m} p_{mn}^L \nabla \Psi_{mn}(\mathbf{r}) + \sum_{n=1}^{N_L^0} r_n^L \nabla \Psi_n(\mathbf{r}), \tag{29}$$

$$\mathbf{H}_{e,i}^{\mathcal{N}}(\mathbf{r}) = \frac{j}{k_0} \nabla \times \mathbf{E}_{e,i}^{\mathcal{N}}(\mathbf{r}), \tag{30}$$

where M is the maximum number of azimuthal modes. Similarly, for an S-polarized excitation, we use the solution representation

$$\mathbf{E}_{e,Ti}^{\mathcal{N}}(\mathbf{r}) = \sum_{m=0}^{M} \sum_{n=1}^{N_{e,T}^m} p_{mn}^{e,T} \frac{j}{k_0 \varepsilon_{e,i}} \nabla \times \nabla \times \mathbf{A}_{mn}^{2e,i}(\mathbf{r}) + q_{mn}^{e,T} \frac{j}{\varepsilon_{e,i}} \nabla \times \mathbf{A}_{mn}^{1e,i}(\mathbf{r})$$
$$+ \sum_{n=1}^{N_{e,T}^0} r_n^{e,T} \frac{j}{\varepsilon_{e,i}} \nabla \times \mathbf{A}_n^{3e,i}(\mathbf{r}), \tag{31}$$

$$\mathbf{E}_{Li}^{\mathcal{N}}(\mathbf{r}) = \sum_{m=0}^{M} \sum_{n=1}^{N_{Li}^m} p_{mn}^L \nabla \Psi_{mn}(\mathbf{r}), \tag{32}$$

$$\mathbf{H}_{e,i}^{\mathcal{N}}(\mathbf{r}) = \frac{j}{k_0} \nabla \times \mathbf{E}_{e,i}^{\mathcal{N}}(\mathbf{r}), \tag{33}$$

where the scalar potential Ψ_{mn} is now defined by

$$\Psi_{mn}(\mathbf{r}) = \Psi_{m+1}(\boldsymbol{\varrho}, z_n^{\mathrm{L}}) \sin[(m+1)\varphi], \tag{34}$$

with $\Psi_m(\boldsymbol{\varrho}, z_n^{\mathrm{L}})$ as in (27).

Note that the vector functions in terms of which the fields in (28)-(30) and (31)-(33) are expressed, are the so-called lowest order distributed multipoles [35]. The completeness of this system of vector functions in the mean square norm at the particle surface S_{i} has been proven in [35]. This property guarantees the convergence of the approximate solution to the exact solution in any closed domain outside the particle, and in particular, at the unit sphere.

Some remarks are in order:

1. $\mathcal{N}$ is a multi-index incorporating both the maximum number of azimuthal modes M, and the number of discrete sources N_{e}^m, N_{T}^m and N_{L}^m.
2. From (30) and (33) it is apparent that only the transverse field $\mathbf{E}_{\mathrm{Ti}}$ contributes to the magnetic field $\mathbf{H}_{\mathrm{i}}$ inside particle i.
3. In the case of an S-polarized excitation, the azimuthal independent harmonic does not contain the nonlocal term $\nabla\Psi_n(\mathbf{r})$ appearing in (29). The reason is that in this case, there is no normal component of the electric field, and so, the additional boundary condition is not required.

As the electromagnetic fields given by (28)-(30) and (31)-(33) solve the Maxwell equations (6)-(7), we have to determine the amplitudes of the discrete sources

$$\{p_{mn}^{\mathrm{e,T}}, p_{mn}^{\mathrm{L}}, q_{mn}^{\mathrm{e,T}}, r_n^{\mathrm{e,T}}, r_n^{\mathrm{L}}\}$$

such that the boundary conditions (8)-(10) are fulfilled. By means of the generalized point matching technique, we obtain the following relations for computation of the amplitudes:

$$\widehat{\mathbf{n}} \times \int\limits_0^{2\pi} [\mathbf{E}_{\mathrm{Ti}}(\boldsymbol{\varrho}_l, \varphi) + \mathbf{E}_{\mathrm{Li}}(\boldsymbol{\varrho}_l, \varphi) - \mathbf{E}_{\mathrm{e}}(\boldsymbol{\varrho}_l, \varphi)] \mathrm{e}^{-\mathrm{j}m\varphi} \mathrm{d}\varphi$$

$$= \widehat{\mathbf{n}} \times \int\limits_0^{2\pi} \mathbf{E}_0(\boldsymbol{\varrho}_l, \varphi) \mathrm{e}^{-\mathrm{j}m\varphi} \mathrm{d}\varphi, \tag{35}$$

$$\widehat{\mathbf{n}} \times \int\limits_0^{2\pi} [\mathbf{H}_{\mathrm{i}}(\boldsymbol{\varrho}_l, \varphi) - \mathbf{H}_{\mathrm{e}}(\boldsymbol{\varrho}_l, \varphi)] \mathrm{e}^{-\mathrm{j}m\varphi} \mathrm{d}\varphi$$

$$= \widehat{\mathbf{n}}_i \times \int\limits_0^{2\pi} \mathbf{H}_0(\boldsymbol{\varrho}_l, \varphi) \mathrm{e}^{-\mathrm{j}m\varphi} \mathrm{d}\varphi, \tag{36}$$

$$\widehat{\mathbf{n}} \cdot \int\limits_0^{2\pi} [\varepsilon_{\mathrm{b}} \mathbf{E}_{\mathrm{Ti}}(\boldsymbol{\varrho}_l, \varphi) + \varepsilon_{\mathrm{b}} \mathbf{E}_{\mathrm{Li}}(\boldsymbol{\varrho}_l, \varphi) - \varepsilon_{\mathrm{e}} \mathbf{E}_{\mathrm{e}}(\boldsymbol{\varrho}_l, \varphi)] \mathrm{e}^{-\mathrm{j}m\varphi} \mathrm{d}\varphi$$

$$= \widehat{\mathbf{n}} \cdot \int\limits_0^{2\pi} \varepsilon_{\mathrm{e}} \mathbf{E}_0(\boldsymbol{\varrho}_l, \varphi) \mathrm{e}^{-\mathrm{j}m\varphi} \mathrm{d}\varphi, \tag{37}$$

where $\{\boldsymbol{\varrho}_l\}_{l=1}^K$ is the set of matching points distributed in the azimuthal plane $\varphi = \mathrm{const}$ over the surface meridian of the particle. For each m, the numbers of discrete sources and matching points are chosen as

$$2N_{\mathrm{e}}^m + 2N_{\mathrm{Ti}}^m + N_{\mathrm{Li}}^m < 5K, \tag{38}$$

in which case, we are led to an overdetermined system of equations for the amplitudes of the discrete sources. The system of equations is solved by QR matrix factorization for a given set of incident angles θ_0, and simultaneously, for both P- and S-polarized excitations.

Once the amplitudes of the discrete sources are known, the components of the far-field pattern

$$\mathbf{F}(\theta, \varphi) = F_\theta(\theta, \varphi) \widehat{\mathbf{e}}_\vartheta + F_\varphi(\theta, \varphi) \widehat{\mathbf{e}}_\varphi, \tag{39}$$

defined through the relation

$$\mathbf{E}_{\mathrm{e}}(\mathbf{r}) = \frac{\mathrm{e}^{-\mathrm{j}k_{\mathrm{e}}r}}{r} \mathbf{F}(\theta, \varphi) + o\left(\frac{1}{r}\right), \quad r \to \infty, \tag{40}$$

are computed for a P-polarized excitation as

$$F_\theta^P(\theta, \varphi) = jk_e \sum_{m=0}^{M} (j\sin\theta)^m \cos[(m+1)\varphi] \sum_{n=1}^{N_e^m} (p_{mn}^e \cos\theta + q_{mn}^e) e^{-jk_e z_n^e \cos\theta}$$

$$- jk_e \sin\theta \sum_{n=1}^{N_e^0} r_n^e e^{-jk_e z_n^e \cos\theta}, \tag{41}$$

$$F_\varphi^P(\theta, \varphi) = -jk_e \sum_{m=0}^{M} (j\sin\theta)^m \sin[(m+1)\varphi] \sum_{n=1}^{N_e^m} (p_{mn}^e + q_{mn}^e \cos\theta) e^{-jk_e z_n^e \cos\theta} \tag{42}$$

and for an S-polarized excitation as

$$F_\theta^S(\theta, \varphi) = jk_e \sum_{m=0}^{M} (j\sin\theta)^m \sin[(m+1)\varphi] \sum_{n=1}^{N_e^m} (p_{mn}^e \cos\theta - q_{mn}^e) e^{-jk_e z_n^e \cos\theta} \tag{43}$$

$$F_\varphi^S(\theta, \varphi) = jk_e \sum_{m=0}^{M} (j\sin\theta)^m \cos[(m+1)\varphi] \sum_{n=1}^{N_e^m} (p_{mn}^e \cos\theta - q_{mn}^e) e^{-jk_e z_n^e \cos\theta}$$

$$+ jk_e \sin\theta \sum_{n=1}^{N_e^0} r_n^e e^{-jk_e z_n^e \cos\theta}. \tag{44}$$

The differential scattering cross section (DCS) is then calculated as

$$\sigma^{P,S}(\theta, \varphi) = |F_\theta^{P,S}(\theta, \varphi)|^2 + |F_\varphi^{P,S}(\theta, \varphi)|^2, \tag{45}$$

the scattering cross section (SCS) as

$$\sigma_{SCS}^{P,S} = \int_0^{2\pi} \int_0^{\pi} \sigma^{P,S}(\theta, \varphi) \sin\theta d\theta d\varphi, \tag{46}$$

and the extinction cross section for a P- and an S-polarized excitation as

$$\sigma_{ext}^P = -\frac{4\pi}{k_e} Im[F_\theta^P(\pi - \theta_0, \pi)] \tag{47}$$

and

$$\sigma_{ext}^S = \frac{4\pi}{k_e} Im[F_\varphi^S(\pi - \theta_0, \pi)], \tag{48}$$

respectively. From (41)-(44) it is readily seen that the components of the far-field pattern are expressed by finite linear combinations of elementary functions, and there is no integration procedure is required for their computation. Besides, the errors in the solution can be estimated by computing the residual norm of the surface fields at the particle surface S_i.

4. Numerical scheme

In this section we describe the numerical scheme of the discrete sources method. The matrix equations corresponding to the azimuthal-dependent boundary conditions (35)-(37) are

$$\begin{bmatrix} \frac{j}{k_0 \varepsilon_i} W_{mi} & \frac{1}{\varepsilon_i} X_{mi} & T_{mL} & -\frac{j}{k_0 \varepsilon_e} W_{me} & -\frac{1}{\varepsilon_e} X_{me} \\ \frac{j}{k_0 \varepsilon_i} Y_{mi} & \frac{1}{\varepsilon_i} V_{mi} & U_{mL} & -\frac{j}{k_0 \varepsilon_e} Y_{me} & -\frac{1}{\varepsilon_e} V_{me} \\ \frac{j\varepsilon_b}{k_0 \varepsilon_i} \mathcal{W}_{mi} & \frac{\varepsilon_b}{\varepsilon_i} \mathcal{X}_{mi} & \varepsilon_b \mathcal{T}_{mL} & -\frac{j}{k_0} \mathcal{W}_{me} & -\mathcal{X}_{me} \\ -X_{mi} & \frac{j}{k_0 \varepsilon_i} W_{mi} & 0 & X_{me} & -\frac{j}{k_0 \varepsilon_e} W_{me} \\ -V_{mi} & \frac{j}{k_0 \varepsilon_i} Y_{mi} & 0 & V_{me} & -\frac{j}{k_0 \varepsilon_e} Y_{me} \end{bmatrix} \begin{bmatrix} p_{mT} \\ q_{mT} \\ p_{mL} \\ p_{me} \\ q_{me} \end{bmatrix} = \begin{bmatrix} E_{0m,\tau}^P \\ -E_{0m,\varphi}^P \\ E_{0m,n}^P \\ H_{0m,\tau}^P \\ H_{0m,\varphi}^P \end{bmatrix} \tag{49}$$

for a P-polarized excitation, and

$$
\begin{bmatrix}
\frac{j}{k_0\varepsilon_i}W_{mi} & -\frac{1}{\varepsilon_i}X_{mi} & T_{mL} & -\frac{j}{k_0\varepsilon_e}W_{me} & \frac{1}{\varepsilon_e}X_{me} \\[4pt]
\frac{j}{k_0\varepsilon_i}Y_{mi} & -\frac{1}{\varepsilon_i}V_{mi} & U_{mL} & -\frac{j}{k_0\varepsilon_e}Y_{me} & \frac{1}{\varepsilon_e}V_{me} \\[4pt]
\frac{j\varepsilon_b}{k_0\varepsilon_i}\mathcal{W}_{mi} & -\frac{\varepsilon_b}{\varepsilon_i}\mathcal{X}_{mi} & \varepsilon_b\mathcal{T}_{mL} & -\frac{j}{k_0}\mathcal{W}_{me} & \mathcal{X}_{me} \\[4pt]
X_{mi} & \frac{j}{k_0\varepsilon_i}W_{mi} & 0 & -X_{me} & -\frac{j}{k_0\varepsilon_e}W_{me} \\[4pt]
V_{mi} & \frac{j}{k_0\varepsilon_i}Y_{mi} & 0 & -V_{me} & -\frac{j}{k_0\varepsilon_e}Y_{me}
\end{bmatrix}
\begin{bmatrix}
p_{mT} \\ q_{mT} \\ p_{mL} \\ p_{me} \\ q_{me}
\end{bmatrix}
=
\begin{bmatrix}
E^S_{0m,\tau} \\ E^S_{0m,\varphi} \\ E^S_{0m,n} \\ H^S_{0m,\tau} \\ H^S_{0m,\varphi}
\end{bmatrix}
\tag{50}
$$

for an S-polarized excitation. In (49) and (50) we introduced the matrices $W_{me,i} = \left[w^{e,i}_{mln}\right]$, $X_{me,i} = \left[x^{e,i}_{mln}\right]$, $Y_{me,i} = \left[y^{e,i}_{mln}\right]$, $V_{me,i} = \left[v^{e,i}_{mln}\right]$, $T_{mL} = [t^L_{mln}]$, and $U_{mL} = [u^L_{mln}]$ by

$$
w^{e,i}_{mln} = \alpha(\boldsymbol{\varrho}_l)\left[k^2_{e,T}\Phi^{e,i}_{m+2}(\boldsymbol{\varrho}_l, z^{e,T}_n) - k_{e,T}\frac{m+1}{\rho_l}\Phi^{e,i}_{m+1}(\boldsymbol{\varrho}_l, z^{e,T}_n) + k^2_{e,T}\Phi^{e,i}_m(\boldsymbol{\varrho}_l, z^{e,T}_n)\right]
$$

$$
\qquad + \beta(\boldsymbol{\varrho}_l)k^2_{e,T}\frac{z_l - z^{e,T}_n}{\rho_l}\Phi^{e,i}_{m+1}(\boldsymbol{\varrho}_l, z^{e,T}_n),
$$

$$
x^{e,i}_{mln} = \alpha(\boldsymbol{\varrho}_l)k_{e,T}\frac{z_l - z^{e,T}_n}{\rho_l}\Phi^{e,i}_{m+1}(\boldsymbol{\varrho}_l, z^{e,T}_n) - \beta(\boldsymbol{\varrho}_l)k_{e,T}\Phi^{e,i}_{m+1}(\boldsymbol{\varrho}_l, z^{e,T}_n),
$$

$$
y^{e,i}_{mln} = -k_{e,T}\frac{m+1}{\rho_l}\Phi^{e,i}_{m+1}(\boldsymbol{\varrho}_l, z^{e,T}_n) + k^2_{e,T}\Phi^{e,i}_m(\boldsymbol{\varrho}_l, z^{e,T}_n),
$$

$$
v^{e,i}_{mln} = k_{e,T}\frac{z_l - z^{e,T}_n}{\rho_l}\Phi^{e,i}_{m+1}(\boldsymbol{\varrho}_l, z^{e,T}_n),
$$

$$
t^L_{mln} = \alpha(\boldsymbol{\varrho}_l)\left[\frac{m+1}{\rho_l}\Psi_{m+1}(\boldsymbol{\varrho}_l, z^L_n) - k_L\Psi_{m+2}(\boldsymbol{\varrho}_l, z^L_n)\right]
$$

$$
\qquad - \beta(\boldsymbol{\varrho}_l)k_L\frac{z_l - z^L_n}{\rho_l}\Psi_{m+2}(\boldsymbol{\varrho}_l, z^L_n),
$$

$$
u^L_{mln} = \frac{m+1}{\rho_l}\Psi_{m+1}(\boldsymbol{\varrho}_l, z^L_n)
$$

where $\widehat{\boldsymbol{\tau}}(\boldsymbol{\varrho}_l) = \alpha(\boldsymbol{\varrho}_l)\widehat{\boldsymbol{\varrho}} + \beta(\boldsymbol{\varrho}_l)\widehat{\boldsymbol{z}}$ and $\widehat{\mathbf{n}}(\boldsymbol{\varrho}_l) = \beta(\boldsymbol{\varrho}_l)\widehat{\boldsymbol{\varrho}} - \alpha(\boldsymbol{\varrho}_l)\widehat{\boldsymbol{z}}$ are the tangential and normal unit vectors to the meridian of the particle surface at the matching point $\boldsymbol{\varrho}_l$. Moreover, we introduced the amplitude vectors $p_{me,T,L} = [p^{e,T,L}_{mn}]$ and $q_{me,T} = [q^{e,T}_{mn}]$, and the vectors associated to the incident field $E^{P,S}_{0m,\tau} = [e^{P,S}_{0ml,\tau}]$, $E^{P,S}_{0m,n} = [e^{P,S}_{0ml,n}]$, $E^{P,S}_{0m,\varphi} = [e^{P,S}_{0ml,\varphi}]$, $H^{P,S}_{0m,\tau} = [h^{P,S}_{0ml,\tau}]$, and $H^{P,S}_{0m,\varphi} = [h^{P,S}_{0ml,\varphi}]$ by

$$
e^P_{0ml,\tau} = \zeta_{ml}\psi_{ml},
$$

$$
e^P_{0ml,n} = \overline{\zeta}_{ml}\psi_{ml},
$$

$$
e^P_{0ml,\varphi} = \kappa^+_{ml}\psi_{ml}\cos\theta_0,
$$

$$
h^P_{0ml,\tau} = -\sqrt{\varepsilon_e}\alpha(\boldsymbol{\varrho}_l)\kappa^+_{ml}\psi_{ml},
$$

$$
h^P_{0ml,\varphi} = -\sqrt{\varepsilon_e}\kappa^-_{ml}\psi_{ml},
$$

and

$$
e^S_{0ml,\tau} = \alpha(\boldsymbol{\varrho}_l)\kappa^+_{ml}\psi_{ml},
$$

$$
e^S_{0ml,n} = \beta(\boldsymbol{\varrho}_l)\kappa^+_{ml}\psi_{ml},
$$

$$
e^S_{0ml,\varphi} = \kappa^-_{ml}\psi_{ml},
$$

$$
h^S_{0ml,\tau} = \sqrt{\varepsilon_e}\zeta_{ml}\psi_{ml},
$$

$$
h^S_{0ml,\varphi} = \sqrt{\varepsilon_e}\kappa^+_{ml}\psi_{ml}\cos\theta_0,
$$

where (x_n, x_τ, x_φ) are the coordinates of a vector $\mathbf{x}$ in a local orthonormal system $(\widehat{\mathbf{n}}, \widehat{\boldsymbol{\tau}}, \widehat{\boldsymbol{\varphi}})$ attached to the matching point $\boldsymbol{\varrho}_l$, and

$$\kappa_{ml}^{\pm} = J_m(k_e \rho_l \sin\theta_0) \pm J_{m+2}(k_e \rho_l \sin\theta_0),$$

$$\zeta_{ml} = \alpha(\boldsymbol{\varrho}_l)\kappa_{ml}^{-}\cos\theta_0 - 2j\beta(\boldsymbol{\varrho}_l)J_{m+1}(k_e \rho_l \sin\theta_0)\sin\theta_0,$$

$$\overline{\zeta}_{ml} = \beta(\boldsymbol{\varrho}_l)\kappa_{ml}^{-}\cos\theta_0 + 2j\alpha(\boldsymbol{\varrho}_l)J_{m+1}(k_e \rho_l \sin\theta_0)\sin\theta_0,$$

$$\psi_{ml} = (-j)^m \exp(-jk_e z_l \cos\theta_l).$$

The matrices $\mathcal{W}_{me,i}$, $\mathcal{X}_{me,i}$, and $\mathcal{T}_{mL}$ can be obtained from the matrices $W_{me,i}$, $X_{me,i}$, and T_{mL} by interchanging the tangential and the normal unit vectors. For example, for $W_{me,i} = W_{me,i}(\alpha,\beta)$ and $\mathcal{W}_{me,i} = \mathcal{W}_{me,i}(\alpha,\beta)$, we have $\mathcal{W}_{me,i}(\alpha,\beta) = W_{me,i}(\beta,-\alpha)$. Comparing (49) and (50) it is easy to see that the solutions for both polarized excitations can be obtained by solving two systems of equations with the same matrix; by making minor changes in the amplitude vectors and the vectors associated to the incident field, the system of equations for an S-polarized excitation reads as

$$
\begin{bmatrix}
\frac{j}{k_0\varepsilon_i}W_{mi} & \frac{1}{\varepsilon_i}X_{mi} & T_{mL} & -\frac{j}{k_0\varepsilon_e}W_{me} & -\frac{1}{\varepsilon_e}X_{me} \\
\frac{j}{k_0\varepsilon_i}Y_{mi} & \frac{1}{\varepsilon_i}V_{mi} & U_{mL} & -\frac{j}{k_0\varepsilon_e}Y_{me} & -\frac{1}{\varepsilon_e}V_{me} \\
\frac{j\varepsilon_b}{k_0\varepsilon_i}\mathcal{W}_{mi} & \frac{\varepsilon_b}{\varepsilon_i}\mathcal{X}_{mi} & \varepsilon_b\mathcal{T}_{mL} & -\frac{j}{k_0}\mathcal{W}_{me} & -\mathcal{X}_{me} \\
-X_{mi} & \frac{j}{k_0\varepsilon_i}W_{mi} & 0 & X_{me} & -\frac{j}{k_0\varepsilon_e}W_{me} \\
-V_{mi} & \frac{j}{k_0\varepsilon_i}Y_{mi} & 0 & V_{me} & -\frac{j}{k_0\varepsilon_e}Y_{me}
\end{bmatrix}
\begin{bmatrix}
p_{mT} \\ -q_{mT} \\ p_{mL} \\ p_{me} \\ -q_{me}
\end{bmatrix}
=
\begin{bmatrix}
E_{0m,\tau}^{S} \\ -E_{0m,\varphi}^{S} \\ E_{0m,n}^{S} \\ -H_{0m,\tau}^{S} \\ -H_{0m,\varphi}^{S}
\end{bmatrix}
\tag{51}
$$

For the azimuthal-independent boundary conditions, the matrix equations for P- and S-polarized excitations are

$$
\begin{bmatrix}
\frac{j}{k_0\varepsilon_i}\overline{W}_i & \overline{T}_L & -\frac{j}{k_0\varepsilon_e}\overline{W}_e \\
\frac{j\varepsilon_b}{k_0\varepsilon_i}\overline{\mathcal{W}}_i & \varepsilon_b\overline{T}_L & -\frac{j}{k_0}\overline{\mathcal{W}}_e \\
\overline{V}_i & 0 & -\overline{V}_e
\end{bmatrix}
\begin{bmatrix}
r_T \\ r_L \\ r_e
\end{bmatrix}
=
\begin{bmatrix}
E_{0,\tau}^{P} \\ E_{0,n}^{P} \\ H_{0,\varphi}^{P}
\end{bmatrix}
\tag{52}
$$

and

$$
\begin{bmatrix}
\frac{1}{\varepsilon_i}\overline{V}_i & -\frac{1}{\varepsilon_e}\overline{V}_e \\
\frac{j}{k_0\varepsilon_i}\overline{W}_i & -\frac{j}{k_0\varepsilon_e}\overline{W}_e
\end{bmatrix}
\begin{bmatrix}
r_T \\ r_e
\end{bmatrix}
=
\begin{bmatrix}
E_{0,\varphi}^{S} \\ H_{0,\tau}^{S}
\end{bmatrix},
\tag{53}
$$

respectively. In (52) and (53), the matrices $\overline{W}_{e,i} = \left[\overline{w}_{ln}^{e,i}\right]$, $\overline{V}_{e,i} = \left[\overline{v}_{ln}^{e,i}\right]$ and $\overline{T}_L = [\overline{t}_{ln}^{L}]$ are defined by

$$\overline{w}_{ln}^{e,i} = \beta(\boldsymbol{\varrho}_l)\left[k_{e,T}^2 \frac{(z_l - z_n^{e,T})^2}{\rho_l^2}\Phi_2^{e,i}(\boldsymbol{\varrho}_l, z_n^{e,T}) + \frac{k_{e,T}}{\rho_l}\Phi_1^{e,i}(\boldsymbol{\varrho}_l, z_n^{e,T}) + k_{e,T}^2 \Phi_0^{e,i}(\boldsymbol{\varrho}_l, z_n^{e,T})\right],$$

$$+ \alpha(\boldsymbol{\varrho}_l)k_{e,T}^2 \frac{z_l - z_n^{e,T}}{\rho_l}\Phi_2^{e,i}(\boldsymbol{\varrho}_l, z_n^{e,T}),$$

$$\overline{v}_{ln}^{e,i} = k_{e,T}\Phi_1^{e,i}(\boldsymbol{\varrho}_l, z_n^{e,T}),$$

$$\overline{t}_{ln}^{L} = -k_L\left[\alpha(\boldsymbol{\varrho}_l) + \beta(\boldsymbol{\varrho}_l)\frac{z_l - z_n^{L}}{\rho_l}\right]\Psi_1(\boldsymbol{\varrho}_l, z_n^{L}),$$

$r_{e,T}$ and r_L are the amplitude vectors $r_{e,T} = [r_n^{e,T}]$ and $r_L = [r_n^{L}]$, respectively, and the vectors associated to the incident field $E_{0,\tau}^{P} = [e_{0l,\tau}^{P}]$, $E_{0,n}^{P} = [e_{0l,n}^{P}]$, $E_{0,\varphi}^{S} = [e_{0l,\varphi}^{S}]$, $H_{0,\tau}^{S} = [h_{0l,\tau}^{S}]$, and $H_{0,\varphi}^{P} = [h_{0l,\varphi}^{P}]$ are defined by

$$e_{0l,\tau}^{P} = [j\alpha(\boldsymbol{\varrho}_l)\cos\theta_0 J_1(k_e \rho_l \sin\theta_0) - \beta(\boldsymbol{\varrho}_l)\sin\theta_0 J_0(k_e \rho_l \sin\theta_0)]\psi_{0l},$$

$$e_{0l,n}^{P} = [j\beta(\boldsymbol{\varrho}_l)\cos\theta_0 J_1(k_e \rho_l \sin\theta_0) + \alpha(\boldsymbol{\varrho}_l)\sin\theta_0 J_0(k_e \rho_l \sin\theta_0)]\psi_{0l},$$

$$h_{0l,\varphi}^{P} = -j\sqrt{\varepsilon_e}J_1(k_e \rho_l \sin\theta_0)\psi_{0l},$$

$$e_{0l,\varphi}^{S} = jJ_1(k_e \rho_l \sin\theta_0)\psi_{0l},$$

$$h_{0l,\tau}^{S} = -\sqrt{\varepsilon_e}\left[j\alpha(\boldsymbol{\varrho}_l)\cos\theta_0 J_1(k_e \rho_l \sin\theta_0) - \beta(\boldsymbol{\varrho}_l)\sin\theta_0 J_0(k_e \rho_l \sin\theta_0)\right]\psi_{0l},$$

with

$$\psi_{0l} = \exp(-jk_e z_l \cos\theta_l).$$

As before, the matrices $\overline{\mathcal{W}}_{e,i}$ can be obtained from the matrices $\overline{W}_{e,i}$ by interchanging the tangential and the normal unit vectors.

The numerical scheme of the discrete sources method involves the following steps.

1. Estimate the number of Fourier harmonics M by imposing that the relative approximation error in (18) is less than 0.05%; M depends on the particle size in the XY plane, the wavenumber of the background medium k_e, and the incident angle θ_0 (which is close to 90°).
2. Evaluate the number of matching points K distributed over the surface meridian; K depends on the exciting wavelength, the meridian length, and the longitudinal wavenumber k_L. Generate the set of the matching points $\{\varrho_l\}_{l=1}^K$, and compute the corresponding tangential unit vectors $\{\widehat{\tau}_l\}_{l=1}^K$.
3. For the azimuthal mode m, chose the number of discrete sources N_e^m, N_T^m, and N_L^m. The numbers of discrete sources for representing the scattered and internal fields can be different; as a rule, their values are between $K/7 - K/3$. The coordinates of the discrete sources are located either on the axis of symmetry Oz, or in the adjoined complex plane [35].
4. For the azimuthal-dependent harmonics, compute the matrix (51), factorize it by using the QR algorithm, calculate the vectors corresponding to the incident field, and for a specified set of incident angles, determine the amplitudes of the discrete sources $\{p_{mn}^{e,T}, p_{mn}^L, q_{mn}^{e,T}\}$.
5. For the azimuthal-independent harmonics, apply the same technique to the matrices (52) and (53), and determine the amplitudes of the discrete sources $\{r_n^{e,T}, r_n^L\}$.
6. Compute the scattering characteristics, and estimate the residual of the surface fields in mean square norm at the particle surface if it is required.

We conclude this section by presenting the modification of the above numerical scheme in the case of a linear dimer. A linear dimmer consists of two axisymmetric particles deposited on the Oz axis (the axis of symmetry of both particles). The domains of the particles are D_i^1 and D_i^2, and their surfaces are denoted by S_i^1 and S_i^2. In this case, the corresponding boundary conditions enforced at S_i^1 and S_i^2 are

$$\widehat{\mathbf{n}}_{1,2} \times [\mathbf{E}_i^{1,2} - (\mathbf{E}_e^1 + \mathbf{E}_e^2)] = \widehat{\mathbf{n}}_{1,2} \times \mathbf{E}_0, \tag{54}$$

$$\widehat{\mathbf{n}}_{1,2} \times [\mathbf{H}_i^{1,2} - (\mathbf{H}_e^1 + \mathbf{H}_e^2)] = \widehat{\mathbf{n}}_{12} \times \mathbf{H}_0, \tag{55}$$

$$\varepsilon_b \widehat{\mathbf{n}}_{1,2} \cdot \mathbf{E}_i^{1,2} = \varepsilon_e \widehat{\mathbf{n}}_{1,2} \cdot [(\mathbf{E}_e^1 + \mathbf{E}_e^2) + \mathbf{E}_0]. \tag{56}$$

From (54)-(56) it is apparent that the electromagnetic interaction between the particles is through the scattered fields only. Following the procedure described above, we obtain an azimuthal-dependent matrix equation which is similar to (49). To present this matrix equation in full detail we introduce the matrices

$$\mathcal{E}_{mi}^j = \begin{bmatrix} \frac{j}{k_0 \varepsilon_i} W_{mi}^j & \frac{1}{\varepsilon_i} X_{mi}^j & T_{mL}^j \\ \frac{j}{k_0 \varepsilon_i} Y_{mi}^j & \frac{1}{\varepsilon_i} V_{mi}^j & U_{mL}^j \\ \frac{j\varepsilon_b}{k_0 \varepsilon_i} \mathcal{W}_{mi}^j & \frac{\varepsilon_b}{\varepsilon_i} \mathcal{X}_{mi}^j & \varepsilon_b \mathcal{T}_{mL}^j \end{bmatrix}, \quad \mathcal{E}_{me}^j = \begin{bmatrix} \frac{j}{k_0 \varepsilon_e} W_{me}^j & \frac{1}{\varepsilon_e} X_{me}^j \\ \frac{j}{k_0 \varepsilon_e} Y_{me}^j & \frac{1}{\varepsilon_e} V_{me}^j \\ \frac{j}{k_0} \mathcal{W}_{me}^j & \mathcal{X}_{me}^j \end{bmatrix}, \tag{57}$$

and

$$\mathcal{H}_{me,i}^j = \begin{bmatrix} -X_{me,i}^j & \frac{j}{k_0 \varepsilon_{e,i}} W_{me,i}^j \\ -V_{me,i}^j & \frac{j}{k_0 \varepsilon_{e,i}} Y_{me,i}^j \end{bmatrix}.$$

Here, the index $j = 1, 2$ referrers to the particle j with domain D_i^j and surface S_i^j. In terms $\mathcal{E}_{me,i}^j$ and $\mathcal{H}_{me,i}^j$, the matrix associated to the dimer is

$$\begin{bmatrix} \mathcal{E}_{mi}^1 & 0 & -\mathcal{E}_{me}^1 & -\mathcal{E}_{me}^2 \\ \mathcal{H}_{mi}^1 & 0 & -\mathcal{H}_{me}^1 & -\mathcal{H}_{me}^2 \\ 0 & \mathcal{E}_{mi}^2 & -\mathcal{E}_{me}^1 & -\mathcal{E}_{me}^2 \\ 0 & \mathcal{H}_{mi}^2 & -\mathcal{H}_{me}^1 & -\mathcal{H}_{me}^2 \end{bmatrix}. \tag{58}$$

Thus, the first two lines correspond to the matching points distributed over the meridian of S_i^1 while the last two lines are associated to S_i^2. Similar representations can be obtained for the azimuthal-independent matrix equations (52) and (53).

5. Numerical analysis

Prior to presenting results for nonspherical particles we like to demonstrate the validity of the developed DSM model by comparing to an extended Mie theory. Actually, comparison of the results between the DSM model and the analytic solution
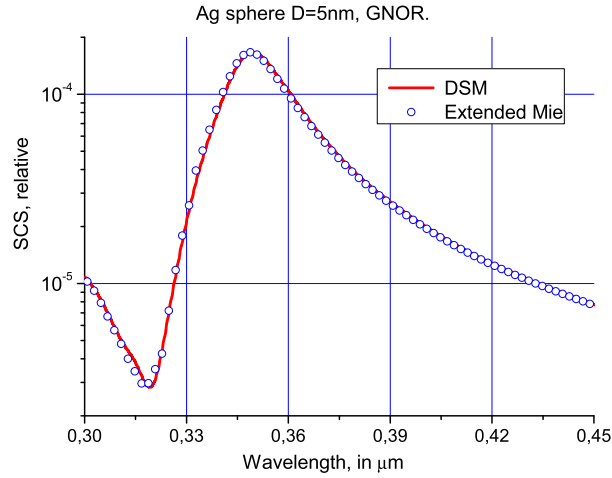
Fig. 2. Scattering cross sections vs wavelength computed by GNOR-DSM and GNOR-Mie for a 5 nm Ag sphere. The parameters are $\hbar\omega_p = 8.99$ eV, $\hbar\gamma = 0.025$ eV, $v_F = 1.39$ µm/s, $D = 3.61 \cdot 10^8$ µm^2/s.
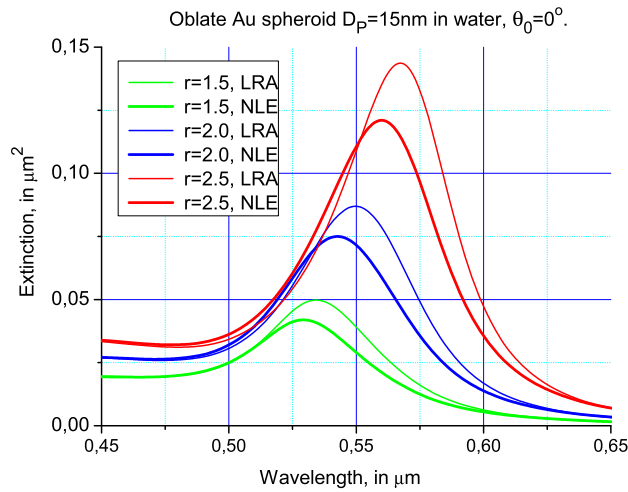

Fig. 3. Extinction cross sections vs exciting wavelength λ computed by LRA and GNOR. The geometrical parameters are $r = b/a$ and $\theta_0 = 0^0$. The background medium is water ($n_e = \sqrt{\varepsilon_e} = 1.33$). (For interpretation of the colors in the figure(s), the reader is referred to the web version of this article.)

based on extension of Mie theory incorporated GNOR (based on Raza [39]) for a Ag sphere $D = 5$ nm can be seen at Fig. 2. The parameters of the Ag sphere have chosen from Raza et al. [12]

$$\hbar\omega_p = 8.99 \text{ eV}, \quad \hbar\gamma = 0.025 \text{ eV}, \quad v_F = 1.39 \text{ µm/s}, \quad D = 3.61 \cdot 10^8 \text{ µm}^2/s.$$

Fig. 2 demonstrates very good agreement between these two methods.

To demonstrate the capability of the proposed method we analyze the scattering by plasmonic metallic spheroids. We start with an oblate spheroid which surface can be described in the cylindrical coordinate system as $\frac{\rho^2}{b^2} + \frac{z^2}{a^2} = 1$, $b > a$. The oblate spheroid has an equivolume diameter of $D_p = 15$ nm. The material of the spheroid is gold (Au). For this metal, the frequency dependent refractive indices $n_i = \sqrt{\varepsilon_i}$ are taken from [36]. We use the GNOR model as NLE and the corresponding parameters for Au are [12]:

$$\hbar\omega_p = 9.02 \text{ eV}, \quad \hbar\gamma = 0.071 \text{ eV}, \quad v_F = 1.39 \text{µm/s}, \quad D = 1.90 \cdot 10^8 \text{µm}^2/s.$$

The main numerical problem of simulating the non-local response is the large difference between the longitudinal k_L and k_T transverse wavenumbers. The ratio $|k_L| / |k_T|$ can reach a value of 60 [29], while the ratio between k_T and k_e is only of about 10. For this reason, the number of matching points for the NLE case is larger than that for the LRA.

In Fig. 3, we plot the extinction cross-sections computed by means of LRA and GNOR models for a gold oblate spheroid. For an aspect ratio $r = 2$, the half-axes of the spheroid are $a = 4.7$ nm and $b = 9.4$ nm. The background medium is water ($n_e = \sqrt{\varepsilon_e} = 1.33$). For the case of an oblate spheroid ($a < b$), the discrete sources are distributed on the imaginary axis of

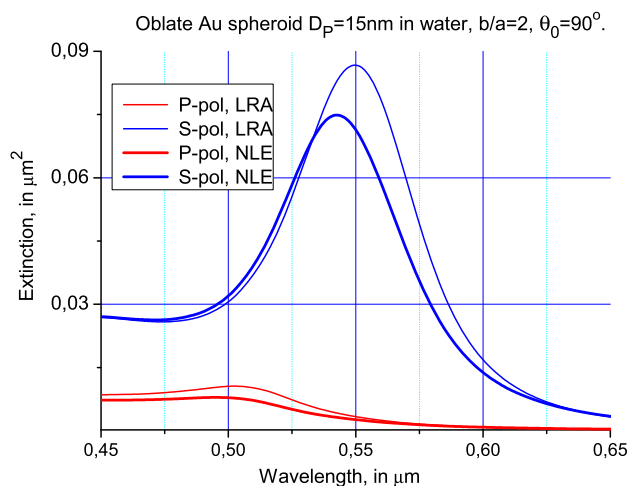Oblate Au spheroid D_P=15nm in water, b/a=2, θ_0=90°.

Fig. 4. Extinction cross sections computed by LRA and NLE for P and S polarized excitation. The geometrical parameters are $r = b/a = 2$ and $\theta_0 = 90°$. The background medium is water.

the spheroid [35]. The results show an increase of $\sigma_{\text{ext}}^{\text{P}}$ with respect to the aspect ratio r. The results show a blue shift and a plasmon mode damping for NLE compared to LRA [8].

In Fig. 4, we plot the extinction cross-sections computed by means of LRA and NLE models. The aspect ratio is $r = 2$, and the incident angle is $\theta_0 = 90°$. In this case, $\sigma_{\text{ext}}^{\text{S}}$ exceeds the value of $\sigma_{\text{ext}}^{\text{P}}$ by several orders. This is because for an S-polarized excitation, the electric field vector $\mathbf{E}_0$ is parallel with the larger axis of the spheroid, while for a P-polarized excitation, it is collinear with the smaller axis of the spheroid. Nevertheless, the blue shift and the plasmon mode damping for NLE as compared to LRA are apparent in both cases.

The computer model has been implemented in Fortran 90. For computations, we used a Notebook Lenovo X280 with Intel Core i7 8550U, 1.80GHz. The time for computing the results in Fig. 4 for a frequency domain ranging from 400 nm to 700 nm, with a step of 5 nm, is 137 sec. The corresponding number of Fourier harmonics is $M = 2$ (plus two phi-independent for P/S polarization). This choice guarantees a plane wave approximation with a relative error of 0.032%. The number of matching points is $K = 372$, and the numbers of discrete sources are $N_e = N_T = N_L = 75$ (for each harmonic, the dimension of the matrix is 1860×375). The distribution of the matching points $\{\varrho_l\}_{l=1}^K$ over the spheroid surface, and the generation of the positions of the discrete sources $\{z_n\}_{n=1}^N$ has been done via the algorithm described in [37].

In the last step of our numerical analysis, we consider the scattering by a linear dimmer. The dimer consists of two gold prolate spheroids with the same equivolume diameter $D_p = 15$ nm, placed in water. In [38], it has been found that for this particular scattering problem, the plasmonic resonance corresponding to LRA is more pronounced for a P-polarized excitation and an incident angle of $\theta_0 = 90°$ (the incident electric field $\mathbf{E}_0$ is parallel to the Oz axis – the axis of symmetry of the prolate spheroids characterized by $a > b$). For this reason, the incident angle is chosen as $\theta_0 = 90°$. The variations of the extinction cross-sections with respect to the aspect ratio $r = a/b$ and the gap size d are illustrated in Figs. 5 and 6. Besides, the blue shift and the plasmon mode damping increase when the aspect ratio r increases, or the gap size d decreases.

Note that in the case $r = 2$, the half-axes of the spheroid are $a = 12$ nm, $b = 6$ nm. The time for computing the results shown in Fig. 6 for $d = 2$ nm and a frequency domain ranging from 450 nm to 750 nm, with a step of 5 nm, is 87 sec. The number of Fourier harmonics is $M = 1$ (plus two phi-independent for P/S polarization), the number of matching points is $K = 312$, and finally, the numbers of discrete sources are $N_e = N_T = N_L = 36$ (for each harmonic, the dimension of the matrix is 1560×230).

6. Conclusions

An extended numerical model of the discrete sources method including non-local effect models has been applied to analyze the scattering by plasmonic axisymmetric particles. In the framework of the new model, the discrete sources for approximating the transverse field (curl and double curl of vector potentials) and the longitudinal field (gradient of scalar potentials) are constructed based on the system of lowest order distributed multipoles [35]. A detailed description of the corresponding numerical scheme has been provided. It was demonstrated that essentially, the same scheme can be used to handle a single particle or a system of two particles (dimmer).

The extinction cross sections of a gold oblate spheroid and a dimer consisting of two identical metallic prolate spheroids have been computed in the frequency domain for different spheroid aspect ratios and gap sizes. Comparing the results obtained by the discrete sources method with the generalized non-local optical response model and those with the local-response approximation, a blue shift and a plasmon mode damping have been confirmed.
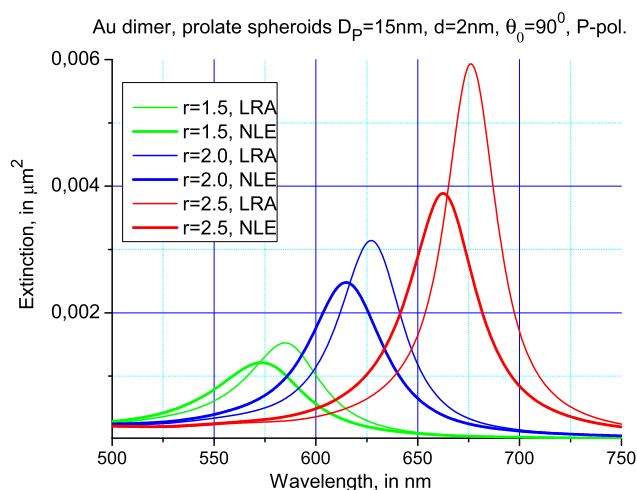
Fig. 5. Extinction cross sections vs exciting wavelength λ for different aspect ratios r. The results are computed by LRA and GNOR for a gold dimer in water with a gap size $d = 2$ nm.
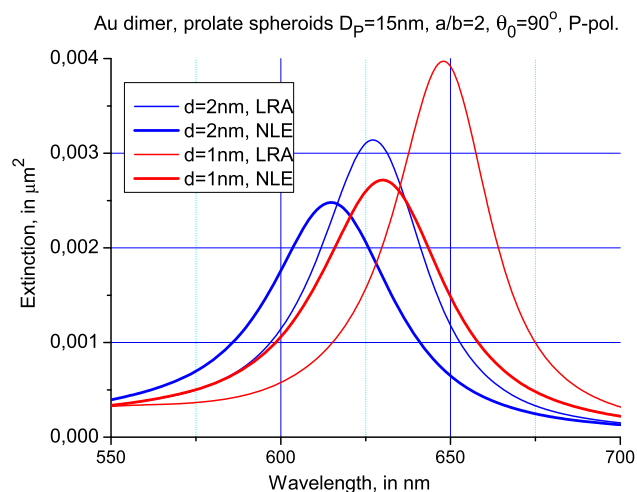

Fig. 6. Extinction cross sections for different gap sizes d. The results are computed by LRA and GNOR for gold spheroids in water with an aspect ratio $r = 2$.

Acknowledgement

References

[1] S.A. Maier, Plasmonics: Fundamentals and Applications, Springer, 2007.
[2] M. Pelton, G. Bryant, Introduction to Metal-Nanoparticle Plasmonics, John Wiley & Sons, 2013.
[3] R.W. Boyd, Nonlinear Optics, Academic Press, New York, 2008.
[4] S.I. Bozhevolnyi, N.A. Mortensen, Plasmonics for emerging quantum technologies, Nanophotonics 6 (5) (2017) 1185–1188.
[5] D. Sarid, W.A. Challener, Modern Introduction to Surface Plasmons: Theory, Mathematica Modeling, and Applications, Cambridge University Press, 2010.
[6] F.J. García de Abajo, Nonlocal effects in the plasmons of strongly interacting nanoparticles, dimers, and waveguides, J. Phys. Chem. C 112 (46) (2008) 17983–17987.
[7] S. Raza, G. Toscano, A-P. Jauho, M. Wubs, N.A. Mortensen, Unusual resonances in nanoplasmonic structures due to nonlocal response, Phys. Rev. B 84 (2011) 121412(R).
[8] M. Wubs, N.A. Mortensen, Nonlocal response in plasmonic nanostructures, in: S.I. Bozhevolnyi, et al. (Eds.), Quantum Plasmonics, Springer, Switzerland, 2017, pp. 279–302.
[9] C. David, F.J. García de Abajo, Spatial nonlocality in the optical response of metal nanoparticles, J. Phys. Chem. C 115 (40) (2011) 19470–19475.
[10] G. Toscano, J. Straubel, A. Kwiatkowski, C. Rockstuhl, F. Evers, H. Xu, N.A. Mortensen, M. Wubs, Resonance shifts and spill-out effects in self-consistent hydrodynamic nanoplasmonics, Nat. Commun. 6 (2015) 7132.
[11] N.A. Mortensen, Nonlocal formalism for nanoplasmonics: phenomenological and semi-classical considerations, Photonics Nanostruct. 11 (4) (2013) 303–309.
[12] S. Raza, S.I. Bozhevolnyi, M. Wubs, N.A. Mortensen, Nonlocal optical response in metallic nanostructures, in: Topical Review, J. Phys. Condens. Matter 27 (18) (2015) 3204–3300.

[13] N.A. Mortensen, S. Raza, M. Wubs, T. Søndergaard, S.I. Bozhevolnyi, A generalized non-local optical response theory for plasmonic nanostructures, Nat. Commun. 5 (2014) 3809–3815.
[14] T. Christensen, W. Yan, A.-P. Jauho, M. Soljačić, N.A. Mortensen, Quantum corrections in nanoplasmonics: shape, scale, and material, Phys. Rev. Lett. 118 (15) (2017) 157402.
[15] Y. Luo, A.I. Fernandez-Dominguez, A. Wiener, S.A. Maier, J.B. Pendry, Surface plasmons and nonlocality: a simple model, Phys. Rev. Lett. 111 (9) (2013) 093901.
[16] W. Yan, M. Wubs, N.A. Mortensen, Projected dipole model for quantum plasmonics, Phys. Rev. Lett. 115 (13) (2015) 137403.
[17] B. Gallinet, J. Butet, O.J.F. Martin, Numerical methods for nanophotonics: standard problems and future challenges, Laser Photonics Rev. 9 (6) (2015) 577–603.
[18] A. Taflove, S.C. Hagness, Computational Electrodynamics - The Finite-Difference Time-Domain Method, third edition, Artech House Publishers, 2005.
[19] J.M. Jin, The Finite Element Method in Electromagnetics, 3rd edition, Wiley-IEEE Press, 2014.
[20] K. Busch, M. König, J. Niegemann, Discontinuous Galerkin methods in nanophotonics, Laser Photonics Rev. 5 (6) (2011) 773–809.
[21] N.C. Nguyen, J. Peraire, B. Cockburn, Hybridizable discontinuous Galerkin methods for the time-harmonic Maxwell's equations, J. Comput. Phys. 230 (19) (2011) 7151–7175.
[22] L. Li, S. Lanteri, R. Perrussel, A hybridizable discontinuous Galerkin method combined to a Schwarz algorithm for the solution of 3d time-harmonic Maxwell's equation, J. Comput. Phys. 256 (1) (2014) 563–581.
[23] M. Kahnert, Numerical solutions of the macroscopic Maxwell equations for scattering by non-spherical particles: a tutorial review, J. Quant. Spectrosc. Radiat. Transf. 178 (2016) 22–37.
[24] M.A. Yurkin, Computational approaches for plasmonics, in: F. Della Sala, S. D'Agostino (Eds.), Handbook of Molecular Plasmonics, Pan Stanford Publishing, 2013, pp. 83–135, Chapter: 2.
[25] F.J. García de Abajo, A. Howie, Retarded field calculation of electron energy loss in inhomogeneous dielectrics, Phys. Rev. B 65 (2002) 115418.
[26] N.G. Khlebtsov, T-matrix method in plasmonics: an overview, J. Quant. Spectrosc. Radiat. Transf. 123 (2013) 184–217.
[27] Ch. Hafner, J. Smajic, M. Agio, Numerical methods for the electrodynamic analysis of nanostructures, in: A.K. Ray (Ed.), Nanoclusters and Nanostructured Surfaces, American Scientific Publishers: Valencia, California, USA, 2010, pp. 207–274.
[28] Yu.A. Eremin, A.G. Sveshnikov, Mathematical models in nanooptics and biophotonics problems on the base of Discrete Sources Method, Comput. Math. Math. Phys. 47 (2) (2007) 262–279.
[29] Yu.A. Eremin, T. Wriedt, W. Hergert, Analysis of the scattering properties of 3D non-spherical plasmonic nanoparticles accounting for nonlocal effects, J. Mod. Opt. 65 (15) (2018) 1778–1786.
[30] K.R. Hiremath, L. Zschiedrich, F. Schmidt, Numerical solution of nonlocal hydrodynamic Drude model for arbitrary shaped nano-plasmonic structures using Nédélec finite elements, J. Comput. Phys. 231 (2012) 5890–5896.
[31] Y.Q. Huang, J.C. Li, W. Yang, Theoretical and numerical analysis of a non-local dispersion model for light interaction with metallic nanostructures, Comput. Math. Appl. 72 (2016) 921–932.
[32] N. Schmitt, C. Scheid, S. Lanteri, A. Moreau, J. Viquerat, A DGTD method for the numerical modeling of the interaction of light with nanometer scale metallic structures taking into account non-local dispersion effects, J. Comput. Phys. 316 (1) (2016) 396–415.
[33] L. Li, S. Lanteri, N.A. Mortensen, M. Wubs, A hybridizable discontinuous Galerkin method for solving nonlocal optical response models, Comput. Phys. Commun. 219 (2017) 99–107.
[34] Yu. Eremin, A. Doicu, T. Wriedt, Discrete sources method for modeling the nonlocal optical response of a nonspherical particle dimer, J. Quant. Spectrosc. Radiat. Transf. 217 (2018) 35–44.
[35] A. Doicu, Y. Eremin, T. Wriedt, Acoustic and Electromagnetic Scattering Analysis Using Discrete Sources, Academic Press, NY, Boston, 2000.
[36] P.B. Johnson, R.W. Christy, Optical constants of the noble metals, Phys. Rev. B 6 (1972) 4370–4379.
[37] D. Sukhanov, Yu. Eremin, Wave scattering analysis based on Discrete Sources Method, J. Quant. Spectrosc. Radiat. Transf. 89 (2004) 349–364.
[38] Yu.A. Eremin, N.V. Grishina, E. Eremina, T. Wriedt, Analysis of plasmonic resonances of two paired noble metal spheroids via the discrete sources method, J. Mod. Opt. 60 (7) (2013) 529–537.
[39] S. Raza, Probing Plasmonic Nanostructures with Electron Energy-Loss Spectroscopy, PhD Thesis, Department of Photonics Engineering, Technical University of Denmark, Lyngby, Denmark, 2014.